Available online at www.sciencedirect.com
SCIENCE DIRECT
International Journal of Machine Tools & Manufacture 45 (2005) 497–507
INTERNATIONAL JOURNAL OF MACHINE TOOLS & MANUFACTURE DESIGN, RESEARCH AND APPLICATION
www.elsevier.com/locate/ijmactool

An investigation of the dynamic absorber effect in high-speed machining

G.S. Duncan, M.F. Tummond, T.L. Schmitz*

Department of Mechanical and Aerospace Engineering, University of Florida, Gainesville, FL 32611, USA

Received 10 December 2003; accepted 1 September 2004

Abstract

In order to achieve increased material removal rates in high-speed machining, stable cutting conditions may be selected based on the system dynamics. In this paper, we apply Receptance Coupling Substructure Analysis to develop models for a stacked flexure setup and a spindle-holder–tool assembly in order to investigate the 'dynamic absorber effect' that can improve the system dynamic stiffness and, therefore, increase the critical stability limit in machining. The dynamic absorber effect results from an interaction between modes associated with the individual substructures, e.g. the spindle-holder and tool in the spindle-holder–tool assembly. Experimental results are provided for: (1) a two degree-of-freedom stacked flexure assembly; and (2) a machining center. These results can be considered in the selection of assembly parameters, such as tool overhang length, as well as in the design of spindle, holder, and tool components in order to improve dynamic stiffness and, consequently, material removal rates.

Keywords: High-speed machining; Tuned damper; Receptance coupling substructure analysis; Flexure

1. Introduction

The use of high-speed machining (HSM) has increased in recent years, especially in the aerospace industry [1]. Using HSM, increased material removal rates (MRR) are achieved through a combination of large axial depths of cut and high spindle speeds (provided adequate power is available). One limitation on the allowable axial depth is regenerative chatter, which has been investigated in a number of studies [2–16]. One method of pre-process chatter prediction and avoidance is the well-known stability lobe diagram. Stability lobe diagrams identify stable and unstable cutting zones (separated by stability 'lobes') as a function of the chip width (or axial depth in peripheral end milling), b, and spindle speed. However, the machining models used to produce these diagrams, whether analytic or time-domain, require knowledge of the tool point dynamics. The dynamic response is typically obtained using impact testing, where an instrumented hammer is used to excite the tool at its free end (i.e. the tool point) and the resulting vibration is measured using an appropriate transducer, typically a low mass accelerometer mounted at the tool point. The complex ratio of the frequency domain vibration and force signals is used as input to the stability analysis. It should be noted that the measured frequency response function (FRF) is specific to the selected substructures. Therefore, if the assembly is altered, a new measurement must be performed.

The equation for the limiting axial depth of cut, $b_{\lim}$, at each spindle speed is shown in Eq. (1), where K_s is the specific cutting energy coefficient, m^* is the average number of teeth in the cut (i.e. the radial immersion, expressed in deg or rad, divided by the spacing of the cutter teeth in corresponding units), and $\mathrm{Re}[G_{11}(\omega)]_{\mathrm{Oriented}}$ represents the negative portion(s) of the real part of the oriented tool point FRF [17]. As seen in Eq. (1), $b_{\lim}$ can be increased by increasing the value of $\mathrm{Re}[G_{11}(\omega)]_{\mathrm{Oriented}}$ (note that only the negative portion of the real part of the oriented FRF is considered in the calculation, so 'increasing' this value means we are making it less negative), which leads to higher MRR. The asymptotic critical stability limit, $b_{\lim,\mathrm{crit}}$, gives the maximum axial depth for which the process is stable at all spindle speeds. This axial depth depends on the most negative (or minimum) value of $\mathrm{Re}[G_{11}(\omega)]_{\mathrm{Oriented}}$ as shown

* Corresponding author. Tel.: +1 352 392 8909; fax: +1 352 392 1071.
E-mail address: tschmitz@ufl.edu (T.L. Schmitz).

0890-6955/$ - see front matter © 2004 Published by Elsevier Ltd.
doi:10.1016/j.ijmachtools.2004.09.005

in Eq. (2).

$$b_{\text{lim}} = \frac{-1}{2K_{\text{s}}\,\text{Re}[G_{11}(\omega)]_{\text{Oriented}}m^*} \tag{1}$$

$$b_{\text{lim,crit}} = \frac{-1}{2K_{\text{s}}\,\min(\text{Re}[G_{11}(\omega)]_{\text{Oriented}})m^*} \tag{2}$$

In this paper, we describe a method to increase $b_{\text{lim,crit}}$ by increasing the minimum value of the negative real part of the tool point FRF. This is achieved by matching the fundamental frequency of the cantilevered tool to a natural frequency of the spindle-holder, where the corresponding modification of the assembly dynamics is analogous to the change in assembly response observed when implementing a damped dynamic absorber. Receptance Coupling Substructure Analysis (RCSA) [18–20] is used to: (1) create a model for two single degree-of-freedom (SDOF) flexures stacked in series; and (2) develop a spindle-holder–tool assembly model. The 'dynamic absorber effect', first observed by Davies et al. [21] and Smith et al. [22] for long slender endmills, is initially demonstrated using stacked monolithic flexures and predictions using the RCSA model are verified. Next, the dynamic absorber effect is shown on a high-speed machining center. The RCSA model is again developed and compared to measurement results.

2. Background and notation

Many examples of the use of substructure analysis to predict the dynamic response of complicated assemblies using measurements and/or models of the individual substructures are available in the literature. In these studies, the substructures have been represented by spatial mass, stiffness, and damping data; modal data; or receptances [23–29]. The latter representation is preferred in situations where the assembly receptances are the desired analysis output, as is the case in this research.

The receptance matrix, $G_{jk}(\omega)$, for the assembly shown in Fig. 1 can be expressed as shown in Eq. (3), where ω is the frequency, X_j and Θ_j are the assembly displacement and rotation at coordinate j, and F_k and M_k are the force and moment applied to the assembly at coordinate k. If coordinate j is coincident with coordinate k, the receptance is referred to as a direct receptance; otherwise, it is a cross-receptance. For the purposes of this paper, the nomenclature $G_{jk}(\omega)$ is used to describe the receptances that are produced when two substructures are coupled to produce an assembly.

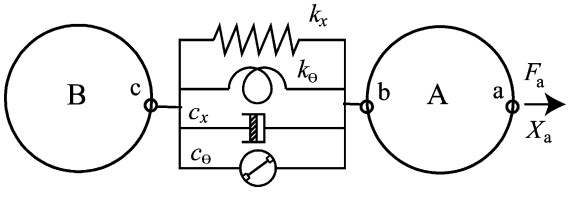

Fig. 1. Receptance coupling model showing the connection of substructures A and B through linear and rotational springs and dampers.

$$G_{jk}(\omega) = \begin{bmatrix} \frac{X_j}{F_k} & \frac{X_j}{M_k} \\ \frac{\Theta_j}{F_k} & \frac{\Theta_j}{M_k} \end{bmatrix} = \begin{bmatrix} H_{jk} & L_{jk} \\ N_{jk} & P_{jk} \end{bmatrix} \tag{3}$$

The substructure receptances, $R_{jk}(\omega)$, are defined in Eq. (4), where x_j and θ_j are the substructure displacement and rotation at coordinate j, and f_k and m_k are the force and moment applied to the substructure at coordinate k [30].

$$R_{jk}(\omega) = \begin{bmatrix} \frac{x_j}{f_k} & \frac{x_j}{m_k} \\ \frac{\theta_j}{f_k} & \frac{\theta_j}{m_k} \end{bmatrix} = \begin{bmatrix} h_{jk} & l_{jk} \\ n_{jk} & p_{jk} \end{bmatrix} \tag{4}$$

Based on the coordinates defined in Fig. 1, the equations to determine the assembly direct receptance, $G_{aa}(\omega)$, is expressed in Eq. (5) as a function of the substructure receptances and linear and rotational stiffness, k_x and k_θ, and viscous damping, c_x and c_θ, terms, which represent the non-rigid connection between substructures [18–20,31].

$$\begin{aligned} G_{aa}(\omega) &= \begin{bmatrix} \frac{X_a}{F_a} & \frac{X_a}{M_a} \\ \frac{\Theta_a}{F_a} & \frac{\Theta_a}{M_a} \end{bmatrix} \\ &= R_{aa}(\omega) - R_{ab}(\omega)[R_{bb}(\omega) + R_{cc}(\omega) \\ &\quad + K^{-1}]^{-1}R_{ba}(\omega) \end{aligned} \tag{5}$$

where

$$K = \begin{bmatrix} k_x + \mathrm{i}c_x\omega & 0 \\ 0 & k_\theta + \mathrm{i}c_\theta\omega \end{bmatrix}$$

Bishop and Johnson [23] presented closed-form receptance functions for the analysis of flexural vibrations of uniform Euler–Bernoulli beams with free, fixed, sliding, and pinned boundary conditions. In this work we apply the Bishop and Johnson expressions for free–free beam receptances to model the holder and tool substructures. As a convenience to the reader, the relevant Bishop and Johnson formulas are included in Appendix A.

3. Flexure investigation

3.1. Model development

The lumped parameter model for the stacked flexure assembly is shown in Fig. 2 (the actual assembly is also pictured). The base flexure, substructure A, is modeled as a SDOF substructure, defined as a mass, m_3, connected to

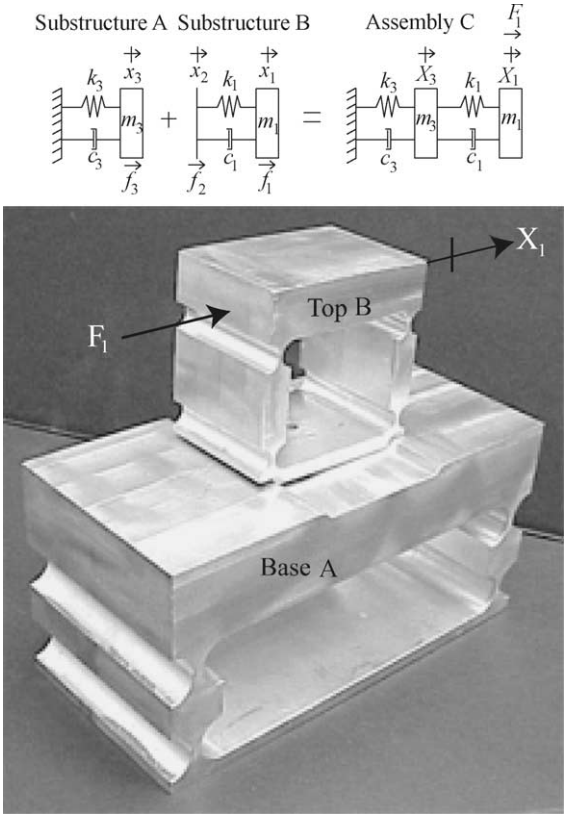

Fig. 2. Lumped parameter stacked flexure model and photograph of 2DOF flexure assembly.

ground through a spring, k_3, and a viscous damper, c_3. The top flexure, substructure B, is modeled with free–free boundary conditions; it consists of a mass, m_1, connected to a massless coordinate, x_2, through a spring, k_1, and viscous damper, c_1. The dynamic response of assembly C to a force, F_1 applied at coordinate X_1 (which represents the uppermost point on the top flexure) is computed using RCSA. It is assumed that the substructure rotational receptances, l_{jk}, n_{jk}, and p_{jk}, are negligible (by design for flexures) and that the substructures are rigidly connected (i.e. $K^{-1}=0$).

The substructure receptances are determined from the lumped parameter equations of motion. For substructure A, the motion is described by Eq. (6). Assuming a harmonic input force $f_3(t)=F_3\,e^{i\omega t}$, the corresponding vibration is $x_3(t)=X_3\,e^{iwt}$ and the direct receptance h_{33} can be defined as shown in Eq. (7).

$$m_3\ddot{x}_3(t)+c_3\dot{x}_3(t)+k_3x_3(t)=f_3(t) \tag{6}$$

$$h_{33}(\omega)=\frac{x_3(\omega)}{f_3(\omega)}=\frac{1}{-\omega^2m_3+i\omega c_3+k_3} \tag{7}$$

Complex matrix inversion is applied to determine h_{12}, h_{21}, h_{11}, and h_{22} for substructure B using the equations of motion provided in Eq. (8). Again assuming a solution of the form $x_j(t)=X_j\,e^{i\omega t}$ for $f_j(t)=F_j\,e^{i\omega t}$, $j=1,2$, Eq. (8) can be written in matrix form as shown in Eq. (9)

$$\begin{aligned} &m_1\ddot{x}_1(t)+c_1\dot{x}_1(t)+k_1x_1(t)-c_1\dot{x}_2(t)-k_1x_2(t)=f_1(t)\\ &-c_1\dot{x}_1(t)-k_1x_1(t)+c_1\dot{x}_2(t)+k_1x_2(t)=f_2(t)\end{aligned} \tag{8}$$

$$\begin{bmatrix} -m_1\omega^2+ic_1\omega+k_1 & -i\omega c_1-k_1\\ -i\omega c_1-k_1 & i\omega c_1+k_1\end{bmatrix}\begin{Bmatrix}x_1\\x_2\end{Bmatrix}=\begin{Bmatrix}f_1\\f_2\end{Bmatrix} \text{ or } [A(\omega)]\{x\}=\{f\} \tag{9}$$

The receptance matrix for substructure B, $G_B(\omega)$, is obtained by inverting the matrix $A(\omega)$ as shown in Eq. (10). The direct and cross-receptances for substructure B are provided in Eqs. (11)–(13).

$$G_B(\omega)=[A(\omega)]^{-1}=\begin{bmatrix}H_{11} & H_{12}\\ H_{21} & H_{22}\end{bmatrix} \tag{10}$$

$$h_{22}=\frac{x_2}{f_2}=\frac{\omega^2m_1-i\omega c_1-k_1}{\omega^2(i\omega m_1c_1+m_1k_1)} \tag{11}$$

$$h_{11}=\frac{-1}{\omega^2m_1} \tag{12}$$

$$h_{12}=\frac{x_1}{f_2}=h_{21}=\frac{x_2}{f_1}=\frac{-1}{\omega^2m_1} \tag{13}$$

Substitution of Eqs. (11)–(13) and Eq. (7) into Eqs. .(4) and (5) with the appropriate coordinate modifications yields the assembly receptance $G_{11}(\omega)$ for a force, F_1, applied at coordinate X_1; see Eq. (14).

$$G_{11}(\omega)=\frac{-1}{\omega^2m_1}-\left(\frac{-1}{\omega^2m_1}\right)\left[\left(\frac{1}{-m_3\omega^2+i\omega c_3+k_3}\right)+\left(\frac{m_1\omega^2-i\omega c_1-k_1}{\omega^2(i\omega m_1c_1+m_1k_1)}\right)\right]^{-1}\left(\frac{-1}{\omega^2m_1}\right) \tag{14}$$

3.2. Experimental results

The 2DOF flexure assembly shown in Fig. 2 was produced by stacking two SDOF flexures. This created a simple dynamic system to experimentally validate the dynamic absorber effect. Three flexures were produced for testing purposes: a top flexure, a large base flexure, and a small base flexure. Flexure theory was used to select the required geometry [32]. The critical geometrical parameters for a notch-hinge flexure are shown in Fig. 3, where s is the depth of the flexure, a_x is the radius of the circular notch-hinge, t is the thickness of the hinge between notches, and L is the vertical distance between notch centerlines. These dimensions for the three flexures are provided in Table 1.

After manufacture, the modal parameters for the flexures were determined by impact testing. For these

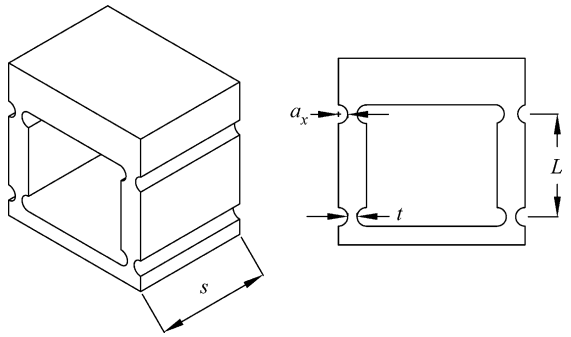

Fig. 3. Design variables for notch-hinge flexure.

measurements, the flexures were adhered to ground with cyanoacrylate (i.e. quick-bonding cement). An impact hammer was used to excite the flexures at their free end (over a bandwidth of approximately 2 kHz) and the response was measured using a low-mass accelerometer. The results are shown in Table 1, where ω_n is the undamped natural frequency.

Modal testing was then performed on the coupled flexures to verify the dynamic absorber effect that takes place when the fundamental cantilevered natural frequencies of the base and top flexures are matched. For all testing, ground was defined as a tombstone with a large mass and stiffness and all connections were made with cyanoacrylate. Fig. 4 displays the displacement-to-force receptances for the large base flexure (connected to ground), the top flexure (connected to ground), and the combined flexures (with the large base flexure connected to ground and the top flexure adhered to the top of the base flexure). From Fig. 4, it can be seen that the natural frequencies of the cantilevered base and top flexures were 408 and 296 Hz, respectively. Even though the natural frequencies are not matched in this case, a 38.5% increase in the minimum real value of the assembly response compared to the top flexure alone is observed. In other words, the addition of a flexible element to the system (i.e. ground was replaced by the base flexure) increased the dynamic stiffness, even in the absence of a direct match between the cantilevered SDOF natural frequencies.

Next, additional weight was added to the large base flexure so that the cantilevered natural frequency was reduced to approach the top flexure natural frequency. Fig. 5 shows the FRFs of the modified large base flexure (connected to ground), the top flexure (connected to ground), and the combined flexures (with the modified base flexure connected to ground and the top flexure attached to the top of the modified base flexure). It can be seen that the natural frequency of the base flexure is now 302 Hz, while the top flexure natural frequency is again 296 Hz. The modes of the individual flexures are now close and interact more strongly. In this case, the minimum value of the assembly FRF real part is 69% larger than the minimum real value of the FRF for the top flexure alone. When matching the natural frequencies of the substructures, the two modes of the combined system split around the original natural frequency and the minimum value of the assembly's negative real response is increased significantly (i.e. made less negative). The base flexure has acted as a 'dynamic absorber' to decrease the assembly response as reflected at the top flexure.

To verify the stacked flexure RCSA model, the model parameters from Table 1 were substituted into $G_{11}(\omega)$, provided in Eq. (14). Fig. 6 displays measured and predicted $G_{11}(\omega)$ results for the stacked flexure system using the large base with added mass. Additional measurements and predictions were completed for the small base flexure and large base flexure with no mass added. Comparable agreement was observed. Discrepancies between actual and predicted results can be attributed to the decision to neglect rotational DOF and the presence of flexibility/damping in the connection between flexures (assumed rigid).

Next, the model parameters were varied to predict $G_{11}(\omega)$ for other cases. Of particular interest was the assembly response when the natural frequencies of the base and top flexures remain matched, as shown in Eq. (15), but the ratio between the base and top flexure mass and spring values was increased by a multiplier value, MV, as shown in Eq. (16).

$$\omega_{n,base} = \sqrt{\frac{k_{base}}{m_{base}}} = \omega_{n,top} = \sqrt{\frac{k_{top}}{m_{top}}} \tag{15}$$

Table 1
Flexure design parameters and results

	s (mm)	L (mm)	a_x (mm)	t (mm)	m (kg)	k (N/m)	c (kg/s)	ω_n (Hz)
Large base flexure								
Modal testing results	90.0	34.76	9.53	3.18	1.43	9.41×10^6	46.9	408.3
Modal testing results with added mass	90.0	34.76	9.53	3.18	2.46	8.85×10^6	70.6	301.9
Small base flexure								
Modal testing results	50.8	38.85	4.76	1.59	0.108	6.34×10^5	4.18	385.0
Modal testing results with added mass	50.8	38.85	4.76	1.59	0.155	5.68×10^5	2.23	304.7
Top flexure								
Modal testing results	50.8	38.85	4.76	1.59	0.145	5.04×10^5	1.17	296.3

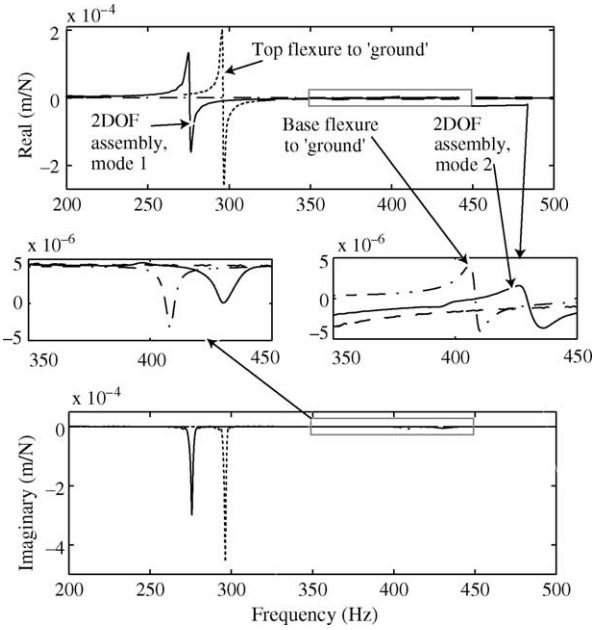

Fig. 4. Combined flexure response, initial cantilevered modes separated.

$$\mathrm{MV} = \frac{k_{\mathrm{base}}}{k_{\mathrm{top}}} = \frac{m_{\mathrm{base}}}{m_{\mathrm{top}}} \tag{16}$$

Fig. 7 displays the real parts of assembly FRFs for the stacked flexure model. It is seen that when MV is equal to 1 (i.e. the base and top flexures are identical), the system has two modes that split around the individual flexure natural frequency (selected to be 300 Hz). As MV increases, the two modes of the coupled flexure system approach each other and, when MV is large enough, the combined response approaches a SDOF system. The minimum value of the negative real part of the assembly FRF increases with MV

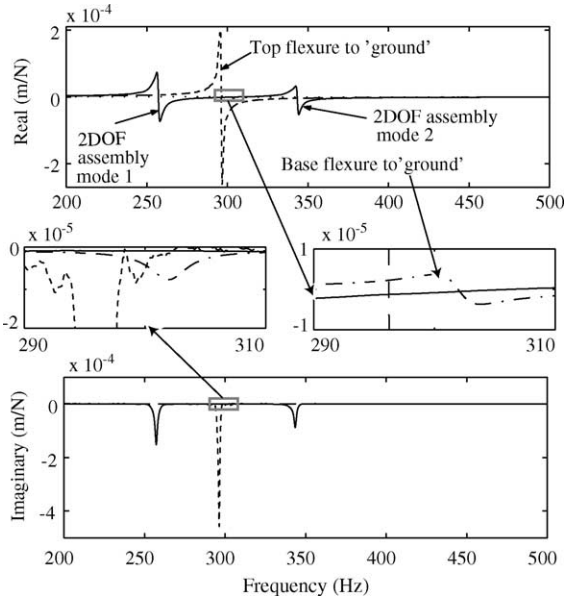

Fig. 5. Combined flexure response, initial cantilevered modes together.

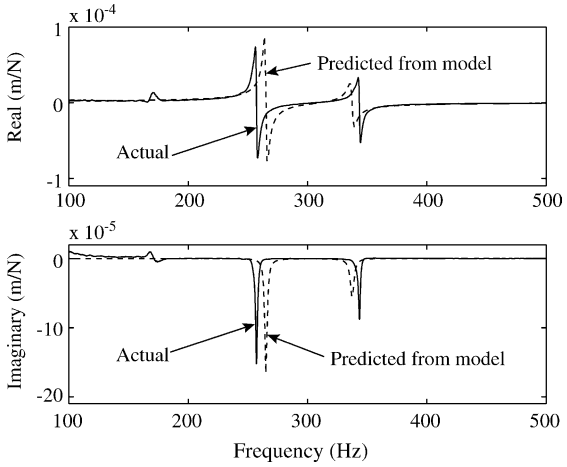

Fig. 6. Measured and predicted $G_{11}(\omega)$ for large base flexure and top flexure with matched natural frequencies.

until the two modes begin to converge to a SDOF and the value of the negative real part begins to decrease again. In other words, the minimum global value of the negative real part of the assembly FRF is not obtained by increasing the mass and stiffness of the base flexure ad infinitum.

The results of the flexure testing and modeling can be extended to the case of the coupled spindle-holder and tool in high-speed machining operations. The fundamental cantilevered tool mode can be considered analogous to the top flexure mode and each spindle-holder mode is analogous to the base flexure mode. As shown in the flexure results, if the fundamental cantilevered tool mode can be matched to a spindle-holder mode, the minimum value of the negative real part of the FRF for the coupled spindle-holder–tool system, as measured at the tool point, can be increased. The dynamic absorber effect that occurs due to the interaction between the modes increases the tool point negative real minimum value relative to the response that would occur if the tool was cantilevered directly to ground (i.e. an infinitely

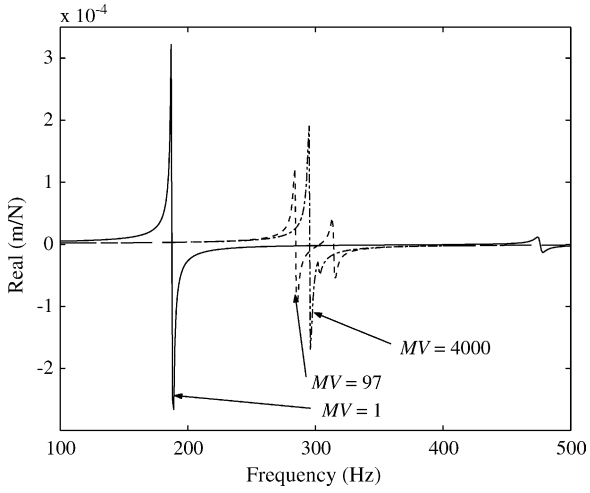

Fig. 7. Coupled flexure FRF real parts for various multiplier values.

stiff spindle-holder). By taking advantage of the dynamic absorber effect, the value for $b_{\text{lim,crit}}$ (see Eq. (2)), can therefore be increased. The tool natural frequency can be varied through tool overhang and/or diameter adjustment, changes in tool material (modulus and density), or manipulation of the connection between the tool and holder.

A second conclusion that can be drawn from this testing is that the largest multiplier value, or greatest mass and stiffness of the base flexure, does not necessarily lead to maximized dynamic stiffness for the coupled flexure system (as reflected at the free end of the top flexure). In terms of a spindle-holder–tool assembly, it can be surmised that during the design of spindles for certain tool geometry ranges, if the interaction between tool and spindle-holder modes is taken into consideration, the stiffest, largest mass spindle may not be the optimum selection for stable machining.

4. Spindle-holder–tool investigation

4.1. Model development

Fig. 8 shows the RCSA model for the spindle-holder–tool assembly. Coordinate X_1 is defined as the assembly tool point and coordinates x_1, x_2, x_3, x_4, and x_5 are the component coordinates. F_1 is the harmonic force applied to the assembly at coordinate X_1, and f_1, f_2, f_3, f_4, and f_5, are the component forces. The component moments are m_2, m_3, m_4, and m_5, and the component rotational displacements are θ_2, θ_3, θ_4, and θ_5. The connection between the tool and inserted shank (i.e. the section of tool inside of holder) includes both linear and rotational springs and viscous dampers, while the connection between the inserted shank and spindle-holder is considered rigid.

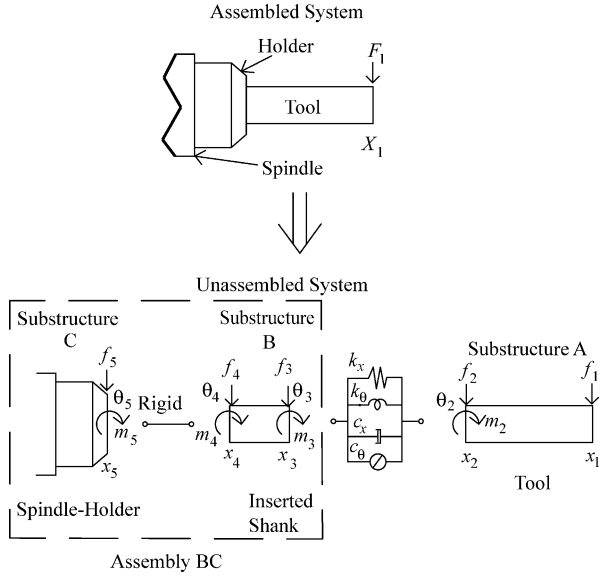

Fig. 8. RCSA model for spindle-holder–tool assembly.

The first step in determining the assembly tool point response is to rigidly couple the spindle-holder to the inserted shank to determine the receptances at coordinate 3, creating assembly BC (see Fig. 8). To determine $G_{33,\text{BC}}(\omega)$, the receptances from Eq. (5) are modified by substituting coordinate 3 for a, coordinate 4 for b, and coordinate 5 for c as shown in Eq. (17). As noted, the term K^{-1} from Eq. (5) is equal to zero for a rigid connection.

$$G_{33,\text{BC}}(\omega) = R_{33} - R_{34}(R_{44} + R_{55})^{-1}R_{43} \tag{17}$$

To determine the inserted shank receptances in Eq. (17) (i.e. right-hand side terms with a subscript of 3 or 4), the inserted shank is assumed to be a free–free beam and the receptances are produced analytically (see Appendix A). However, it is assumed that the entire mass is concentrated at coordinate 5 to simplify the coupling procedure. Therefore, the length of the beam is set to an arbitrarily small length of 1 mm and the density is adjusted to provide the appropriate mass. Although this assumption may impose errors in the model, it is a reasonable approximation for most situations.

To populate the spindle-holder receptance matrix, R_{55}, the displacement-to-force receptance, h_{55}, is first measured at the end of the spindle-holder. To determine l_{55}, n_{55}, and p_{55}, the h_{55} FRF is first fit with modal parameters, $m_{q,i}$, $c_{q,i}$, and $k_{q,i}$, for each mode, i, using a peak picking method [33]. The fit curve is defined according to Eq. (18), where n is the total number of modes in the h_{55} response selected for fitting.

$$h_{55,\text{fit}} = \sum_{i=1}^{n} \frac{1}{k_{q,i} - m_{q,i}\omega^2 + \mathrm{i}c_{q,i}\omega} \tag{18}$$

It is next assumed that each mode of $h_{55,\text{fit}}$ can be approximately represented as a clamped-free Euler–Bernoulli beam with a cylindrical cross-section; the best-fit modal parameters are then converted to represent the geometric properties of this 'artificial' cantilever. Clearly, this approximation is not accurate in all situations, but in the absence of other measurement information it provides a reasonable starting point. The expressions for natural frequency, $\omega_{\text{nC},i}$, dimensionless damping ratio, $\zeta_{\text{C},i}$, and stiffness, $k_{\text{C},i}$ are shown in Eqs. (19)–(21), respectively, where the subscript C refers to the spindle-holder substructure.

$$\omega_{\text{nC},i} = \sqrt{\frac{k_{q,i}}{m_{q,i}}} \tag{19}$$

$$\xi_{\text{C},i} = \frac{c_{q,i}}{\sqrt{2m_{q,i}k_{q,i}}} \tag{20}$$

$$k_{\text{C},i} = 4k_{q,i} \tag{21}$$

The next step is to determine the diameter, $d_{\text{C},i}$, of the artificial cantilever for each fit mode. The equation for the natural frequency of the first mode of a cantilevered

beam is shown in Eq. (22), where λ_F is a constant equal to 1.87510407, $L_{C,i}$ is the beam length, E_s is the modulus of elasticity (steel assumed), $I_{C,i}$ is the second area moment of inertia, and $m_{C,i}$ is the mass per length of the beam [34].

$$\omega_{nC,i} = \frac{\lambda_F^2}{L_{C,i}^2}\sqrt{\frac{E_s I_{C,i}}{m_{C,i}}} \tag{22}$$

Eq. (23) gives $I_{C,i}$ and the expression for $m_{C,i}$ is provided in Eq. (24). Eq. (25) gives $L_{C,i}$, where ρ_s is the density of steel.

$$I_{C,i} = \frac{\pi d_{C,i}^4}{64} \tag{23}$$

$$m_{C,i} = \frac{k_{C,i}}{\omega_{nC,i}^2} \tag{24}$$

$$L_{C,i} = \frac{4m_{C,i}}{\pi d_{C,i}^2 \rho_s} \tag{25}$$

Inserting Eqs. (23)–(25) into Eq. (22) and solving for $d_{C,i}$ yields Eq. (26). Once $d_{C,i}$ is determined, $L_{C,i}$ can be found using Eq. (25). Eq. (27) is then used to determine the structural damping factor, $\eta_{C,i}$.

$$d_{C,i} = \left(\frac{64^2 m_{C,i}^4 \omega_{nC,i}^2}{\lambda_F^4 E_s \pi^4 \rho_s^3}\right)^{0.1} \tag{26}$$

$$\eta_{C,i} = 2\xi_{C,i} \tag{27}$$

After the cantilevered beam parameters are determined, the rotational receptances at coordinate 5 can be determined analytically [23]. Eq. (28) provides the beam constant $\lambda_{C,i}$, where $E_{C,i}$ is the complex modulus of elasticity, defined in Eq. (29), and ω is the frequency. The receptance calculations are shown in Eq. (30).

$$\lambda_{C,i}^4 = \frac{16\omega^2 \rho_s}{E_{C,i} d_{C,i}^2} \tag{28}$$

$$E_{C,i} = E_s(1 + i\eta_{C,i}) \tag{29}$$

$$L_{55,BC} = \sum_{i=1}^{n} \frac{F_{1C,i}}{E_{C,i} I_{C,i} \lambda_{C,i}^2 F_{4C,i}} \tag{30}$$

$$N_{55,BC} = L_{55,BC}$$

$$P_{55,BC} = \sum_{i=1}^{n} \frac{F_{6C,i}}{E_{C,i} I_{C,i} \lambda_{C,i} F_{4C,i}}$$

where

$$F_{1C,i} = \sin \lambda_{C,i} L_{C,i} \sinh \lambda_{C,i} L_{C,i}$$

$$F_{4C,i} = \cos \lambda_{C,i} L_{C,i} \cosh \lambda_{C,i} L_{C,i} + 1$$

$$F_{5C,i} = \cos \lambda_{C,i} L_{C,i} \sinh \lambda_{C,i} L_{C,i} - \sin \lambda_{C,i} L_{C,i} \cosh \lambda_{C,i} L_{C,i}$$

$$F_{6C,i} = \cos \lambda_{C,i} L_{C,i} \sinh \lambda_{C,i} L_{C,i} + \sin \lambda_{C,i} L_{C,i} \cosh \lambda_{C,i} L_{C,i}$$

All the terms are now available to determine $G_{33,BC}(\omega)$ in Eq. (17). This result is then coupled to an analytical model of the overhung portion of the free–free tool (substructure A in Fig. 8), which is developed according to the equations in Appendix A. The assembly expression is provided in Eq. (31). Performing the matrix operations in Eq. (31) and extracting the first row, first column term yields the direct tool point FRF, $G_{ABC,11}(\omega)$, for a harmonic force, F_1, applied at assembly coordinate, X_1.

$$G_{ABC}(\omega) = R_{11} + R_{12}(R_{22} + R_{33,BC} + K^{-1})^{-1} R_{21} \tag{31}$$

The final unknowns in Eq. (31) are the connection stiffness and damping terms that populate the K matrix. To find these values, a single assembly measurement at the tool point is completed and the connection terms are adjusted to provide a match between the predicted and measured assembly responses. The RCSA model can then be used to predict the assembly dynamics after changes to the substructures (e.g. modification of the tool overhang length).

4.2. Spindle-holder–tool experimental results

The goal of this testing was the comparison of two responses: (1) the spindle-holder–tool dynamics as reflected at the tool point when the fundamental cantilever tool mode is matched to a spindle-holder mode; and (2) the tool point response with the tool is connected directly to ground through the same tool-holder connection parameters.

The first step in the RCSA procedure was to measure the displacement-to-force FRF at the free end of the spindle-holder, perform a modal fit, and convert the modal

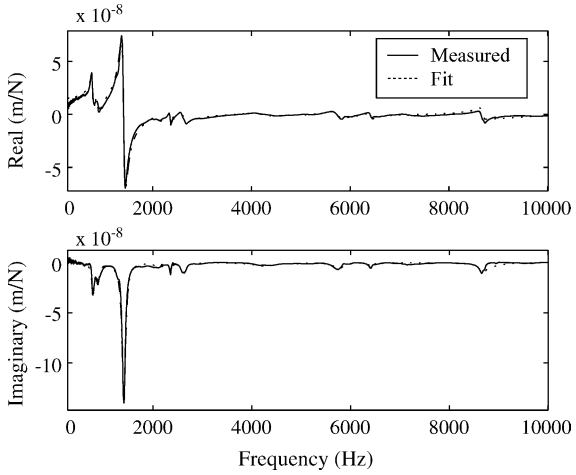

Fig. 9. Spindle-holder FRF with modal fit superimposed.

Table 2
Modal and artificial cantilever parameters for spindle-holder FRF

Mode	m_q (kg)	c_q (kg/s)	k_q (N/m)	d_C (m)	L_C (m)	η_C (–)
1	20.06	6192	4.87×10^8	0.180	0.404	0.063
2	20.68	9575	6.36×10^8	0.187	0.387	0.084
3	1.49	807.9	1.17×10^8	0.072	0.190	0.061
4	13.44	13,485	2.39×10^9	0.187	0.251	0.075
5	37.95	5856	8.32×10^9	0.290	0.295	0.010
6	7.69	5937	2.10×10^9	0.156	0.205	0.047
7	3.31	10,471	2.37×10^9	0.123	0.143	0.118
8	3.38	3661	4.43×10^9	0.132	0.127	0.030
9	8.60	3983	1.40×10^{10}	0.196	0.147	0.012
10	2.32	1796	6.92×10^9	0.123	0.100	0.014

parameters to geometric parameters of an artificial cantilever for each mode within the bandwidth of interest. The FRF of the spindle-holder and the artificial cantilever spindle-holder FRF are displayed in Fig. 9. The holder had a thermal shrink fit tool connection and CAT 40 spindle interface. The modal parameters and the artificial cantilever parameters are provided in Table 2. For the artificial cantilever fits, the modulus of elasticity of steel, E_s, and the density of steel, ρ_s, were taken to be 2.0×10^{11} Pa and 7800 kg/m^3, respectively.

The parameters from Table 2 were next used to generate all four receptances for the spindle-holder free end. Once the spindle-holder receptances were determined, the inserted shank free-free receptances were computed. The tool information is shown in Table 3, where the density was determined by mass and volume measurements and the modulus and structural damping factor were determined by free–free modal testing. The receptances for the spindle-holder-inserted shank at the end of the inserted shank were then determined using Eq. (17).

The final step in determining the RCSA model was to calculate the free–free receptances for the overhung portion of the tool and couple these receptances to the spindle-holder-inserted shank substructure; see Eq. (31). The overhung tool receptances were determined by inserting the tool parameters into the equations in Appendix A. The connection parameters were determined by fitting the predicted FRF to a spindle-holder–tool measurement recorded at a known overhang length. The connection parameters are given in Table 4 and a comparison between the RCSA model and spindle-holder–tool measurement is shown in Fig. 10.

To illustrate the dynamic absorber effect, the free–free overhung tool was coupled to ground using the connection parameters in Table 4. The result is shown in Fig. 11, together with the spindle-holder and spindle-holder–tool FRFs. It is seen that the spindle-holder and grounded overhung tool each have a mode at approximately 1400 Hz. When the two substructures are combined, the modes split around the 1400 Hz frequency and produce a dynamically stiffer two-mode system. The mode at approximately 700 Hz is a spindle-holder mode that has been shifted to a slightly lower frequency and amplified by the addition of the tool to the assembly.

Table 3
Tool information

Tool material	Carbide
Tool length (m)	0.140
Tool diameter (m)	0.019
Number of teeth	4
Overhang length (m)	0.100
Tool mass	0.471
Modulus of elasticity (N/m^2)	5.39×10^{11}
Density (kg/m^3)	14,272
Structural damping factor	0.0015

Table 4
Connection parameters

k_x (N/m)	k_θ (N m/rad)	c_x (kg/s)	c_θ (N m s/rad)
5×10^7	5×10^7	800	800

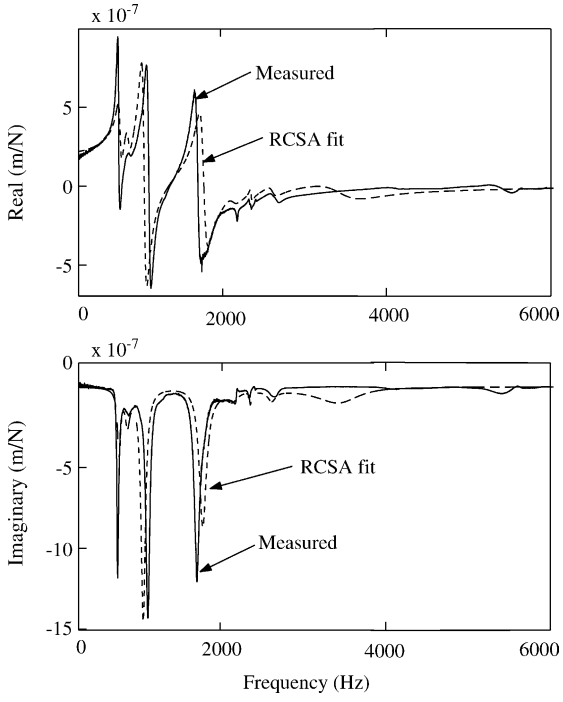

Fig. 10. RCSA model for spindle-holder–tool assembly.

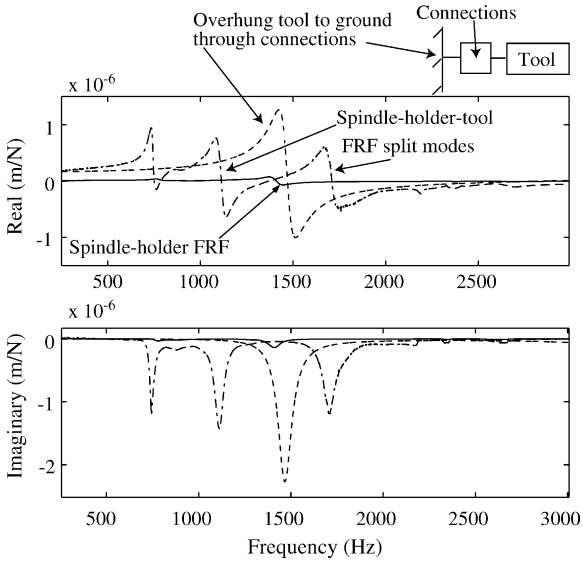

Fig. 11. Spindle-holder–tool dynamic absorber effect.

The spindle-holder–tool testing showed that the dynamic absorber effect that occurs when the fundamental tool natural frequency is matched to a holder-spindle natural frequency can increase the assembly dynamic stiffness at the tool point. In this case, the spindle-holder mode that interacted with the tool mode was fairly flexible (i.e. a low MV value) so the assembly modes are well-separated. It can also be shown that higher MV values produce overlapping modes and improved dynamic stiffness. In Fig. 12, it is seen that increasing the overhang from 106.2 mm (9:1 length to diameter ratio) to 118 mm (10:1) increases the dynamic stiffness due to the dynamic absorber effect in the presence of a high MV spindle mode. The connection parameters for this case are given in Table 5.

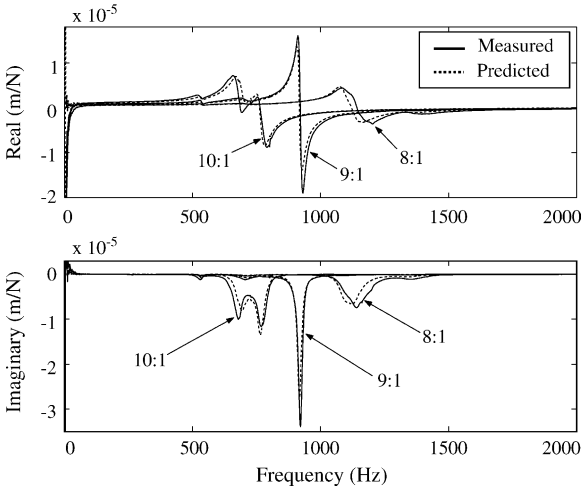

Fig. 12. Example of dynamic absorber effect for 11.8 mm diameter tool in stiff spindle. The tool is dynamically stiffer with the 118 mm overhang (10:1) than with the 106.2 mm overhang (9:1) [19].

Table 5
Connection parameter

k_x (N/m)	k_θ (N m/rad)	c_x (kg/s)	c_θ (N m s/rad)
2.1×10^7	1.4×10^6	130	35

5. Conclusions

This paper described the dynamic absorber effect, where interactions between substructure modes can lead to a dynamically stiffer system. Experimental verification was provided for a simple stacked flexure setup and more complicated spindle-holder–tool assemblies. Receptance Coupling Substructure Analysis (RCSA) models were developed for these cases and were used to predict the assembly responses. It was shown that by taking advantage of the dynamic absorber effect the minimum negative real value of the tool point frequency response function can be made less negative; therefore, the critical stability limit can be increased and higher material removal rates obtained.

Acknowledgements

This work was partially supported by the National Science Foundation under Grant No. DMI-0238019 and the Office of Naval Research (2003 Young Investigator Program). Any opinions, findings, and conclusions or recommendations expressed in this material are those of the authors and do not necessarily reflect the views of the National Science Foundation or Office of Naval Research. The authors also wish to acknowledge Dr. M. Davies, University of North Carolina-Charlotte, Charlotte, NC, for providing the initial description of the 'dynamic absorber effect', and contributions to the development of the RCSA method by Dr. T. Burns, National Institute of Standards and Technology, Gaithersburg, MD.

Appendix A. Free–free beam receptances

Bishop and Johnson [23] showed that the displacement and rotation-to-force and moment receptances for uniform Euler–Bernoulli beams could be represented by simple closed-form expressions. For a cylindrical free-free beam with coordinates j and k identified at each end, the frequency-dependent direct and cross-receptances are given by

$$h_{jj} = h_{kk} = \frac{-F_5}{EI(1+\mathrm{i}\eta)\lambda^3 F_3},$$
$$h_{jk} = h_{kj} = \frac{F_8}{EI(1+\mathrm{i}\eta)\lambda^3 F_3} \quad \text{(A1)}$$

$$l_{jj} = -l_{kk} = \frac{-F_1}{EI(1+\mathrm{i}\eta)\lambda^2 F_3}, \qquad l_{jk} = -l_{kj} = \frac{F_{10}}{EI(1+\mathrm{i}\eta)\lambda^2 F_3} \tag{A2}$$

$$n_{jj} = -n_{kk} = \frac{-F_1}{EI(1+\mathrm{i}\eta)\lambda^2 F_3}, \qquad n_{jk} = -n_{kj} = \frac{-F_{10}}{EI(1+\mathrm{i}\eta)\lambda^2 F_3} \tag{A3}$$

$$p_{jj} = p_{kk} = \frac{F_6}{EI(1+\mathrm{i}\eta)\lambda F_3}, \qquad p_{jk} = p_{kj} = \frac{F_7}{EI(1+\mathrm{i}\eta)\lambda F_3} \tag{A4}$$

where E is the elastic modulus, I is the second area moment of inertia, η is the structural damping factor (damping was not included in Ref. [23], but has been added as part of this analysis), and

$$\lambda^4 = \frac{\omega^2 m}{EI(1+\eta)L} \tag{A5}$$

$$\begin{aligned} F_1 &= \sin\lambda L \sinh\lambda L, \quad F_3 \\ &= \cos\lambda L \cosh\lambda L - 1, \quad F_5 \\ &= \cos\lambda L \sinh\lambda L - \sin\lambda L \cosh\lambda L, \quad F_6 \\ &= \cos\lambda L \sinh\lambda L + \sin\lambda L \cosh\lambda L, \quad F_7 \\ &= \sin\lambda L + \sinh\lambda L, \quad F_8 \\ &= \sin\lambda L - \sinh\lambda L, \quad F_{10} = \cos\lambda L - \cosh\lambda L \end{aligned} \tag{A6}$$

In Eq. (A5), the cylindrical beam mass is given by $m = \pi d_o^2 L\rho/4$, where d_o is the outer diameter, L is the length, and ρ is the density; the cylinder's second area moment of inertia is $I = \pi d_o^4/64$; and ω is the frequency (in rad/s).

References

[1] J. Halley, A. Helvey, S. Smith, W. Winfough, The impact of high-speed machining on the design and fabrication of aircraft components, in: Proceedings of the 17th Biennial Conference on Mechanical Vibration and Noise, ASME Design and Technical Conferences, Las Vegas, Nevada, 12–16 September, 1999.

[2] S. Tobias, W. Fishwick, The chatter of lathe tools under orthogonal cutting conditions, Transactions of the ASME 80 (1958) 1079.

[3] H. Merrit, Theory of self-excited machine tool chatter, ASME Journal of Engineering for Industry 87 (1965) 447–454.

[4] F. Koenisberger, J. Tlusty, Machine Tool Structures—vol. I: Stability Against Chatter, Pergamon Press, Englewood Cliffs, NJ, 1967.

[5] R. Shridar, R. Hohn, G. Long, A stability algorithm for the general milling process, Journal of Engineering for Industry, Transactions of the ASME 90 (1968) 330.

[6] J. Tlusty, W. Zaton, F. Ismail, Stability lobes in milling, Annals of the CIRP 32 (1) (1983) 309–313.

[7] R. King (Ed.), Handbook of High-speed Machining Technology, Chapman & Hall, New York, 1985.

[8] I. Minis, T. Yanushevsky, R. Tembo, R. Hocken, Analysis of linear and nonlinear chatter in milling, Annals of the CIRP 39 (1990) 459–462.

[9] S. Smith, J. Tlusty, An overview of modeling and simulation of the milling process, ASME Journal of Engineering for Industry 113 (1991) 169–175.

[10] T. Delio, J. Tlusty, S. Smith, Use of audio signals for chatter detection and control, ASME Journal of Engineering for Industry 114 (1992) 146–157.

[11] Y. Altintas, E. Budak, Analytical prediction of stability lobes in milling, Annals of the CIRP 44 (1) (1995) 357–362.

[12] Y. Altintas, P. Lee, A general mechanics and dynamics model for helical end mills, Annals of the CIRP 45 (1) (1996) 59–64.

[13] E. Budak, Y. Altinas, Analytical prediction of chatter stability conditions for multi-degree of freedom systems in milling. Part I: modeling; part II: applications, ASME Journal of Dynamic Systems, Measurement, and Control 120 (1998) 22–36.

[14] A. Nayfeh, C. Chin, J. Pratt, Applications of perturbation methods to tool chatter dynamics, in: Dynamics and Chaos in Manufacturing Processes, Wiley, New York, 1997.

[15] M. Davies, B. Balachandran, Impact dynamics in milling of thin-walled structures, Nonlinear Dynamics 22 (2000) 375–392.

[16] P. Bayly, J. Halley, B. Mann, M. Davies, Stability of interrupted cutting by temporal finite element analysis, in: Proceedings of the 18th Biennial Conference on Mechanical Vibration and Noise, ASME Design Engineering Technical Conferences, 9–13 September, 2001, Pittsburgh, PA, paper no. DETC2001/VIB-21581.

[17] J. Tlusty, Manufacturing Processes and Equipment, Prentice Hall, Upper Saddle River, NJ, 2000.

[18] T. Schmitz, R. Donaldson, Predicting high-speed machining dynamics by substructure analysis, Annals of the CIRP 49 (1) (2000) 303–308.

[19] T. Schmitz, M. Davies, M. Kennedy, Tool point frequency response prediction for high-speed machining by RCSA, Journal of Manufacturing Science and Engineering 123 (2001) 700–707.

[20] T. Schmitz, M. Davies, K. Medicus, J. Snyder, Improving high-speed machining material removal rates by rapid dynamic analysis, Annals of the CIRP 50 (1) (2001) 263–268.

[21] M. Davies, B. Dutterer, J. Pratt, A. Schaut, On the dynamics of high-speed milling with long, slender endmills, Annals of the CIRP 47 (1) (1998) 55–60.

[22] S. Smith, W. Winfough, J. Halley, The effect of tool length on stable metal removal rate in high-speed milling, Annals of the CIRP 47 (1) (1998) 307–310.

[23] R.E.D. Bishop, D.C. Johnson, The Mechanics of Vibration, Cambridge University Press, Cambridge, 1960.

[24] W.C. Hurty, Dynamic analysis of structural systems using component modes, AIAA Journal 3 (4) (1965) 678–685.

[25] A.L. Klosterman, J.R. Lemon, Building block approach to structural dynamics, American Society of Mechanical Engineering Annual Vibration Conference, publication VIBR-30, 1969.

[26] B. Jetmundsen, R.L. Bielawa, W.G. Flannelly, Generalized frequency domain substructure synthesis, Journal of the American Helicopter Society 33 (1988) 55–64.

[27] Y. Ren, C.F. Beards, On substructure synthesis with FRF data, Journal of Sound and Vibration 185 (1995) 845–866.

[28] W. Lui, D.J. Ewins, Substructure synthesis via elastic media, Journal of Sound and Vibration 257 (2) (2002) 361–379.

[29] A.S. Yigit, A.G. Ulsoy, Dynamic stiffness evaluation for reconfigurable machine tools including weakly non-linear joint characteristics, Proceedings of the I MECH E Part B Journal of Engineering Manufacture 216 (1) (2002) 87–101.

[30] S. Park, Y. Altintas, M. Movahhedy, Receptance coupling for end mill, Journal of Machine Tools and Manufacture 43 (2003) 889–896.
[31] T. Schmitz, T. Burns, Receptance coupling for high-speed dynamics prediction, in: Proceedings of the 21st International Modal Analysis Conference, 3–6 February, 2003, Kissimmee, FL (on CD).
[32] S. Smith, Flexure Elements of Elastic Mechanisms, Gordon & Breach, Amsterdam, The Netherlands, 2000.
[33] D. Ewins, Modal Testing: Theory and Practice, Research Studies Press, Somerset, England, 1995.
[34] R. Blevins, Formulas for Natural Frequency and Mode Shape, Van Nostrand Reinhold, New York, NY, 1979.